Combustor Turbine Interface Studies—Part 2: Flow and Thermal Field Measurements

W. F. Colban

A. T. Lethander

K. A. Thole

Mechanical Engineering Department,
Virginia Polytechnic Institute and State University,
Blacksburg, VA 24061

G. Zess

Pratt and Whitney,
East Hartford, CT 06108

Most turbine inlet flows resulting from the combustor exit are nonuniform in the near-platform region as a result of cooling methods used for the combustor liner. These cooling methods include injection through film-cooling holes and injection through a slot that connects the combustor and turbine. This paper presents thermal and flow field measurements in the turbine vane passage for a combustor exit flow representative of what occurs in a gas turbine engine. The experiments were performed in a large-scale wind tunnel facility that incorporates combustor and turbine vane models. The measured results for the thermal and flow fields indicate a secondary flow pattern in the vane passage that can be explained by the total pressure profile exiting the combustor. This secondary flow field is quite different than that presented for past studies with an approaching flat plate turbulent boundary layer along the upstream platform. A counter-rotating vortex that is positioned above the passage vortex was identified from the measurements. Highly turbulent and highly unsteady flow velocities occur at flow impingement locations along the stagnation line. [DOI: 10.1115/1.1561812]

Introduction

The flow and thermal fields at the combustor-turbine junction in a gas turbine engine are highly complex and cannot be idealized by a uniform mean field superimposed with high turbulence levels. This is particularly true in the turbine platform region, which has been generally assumed to have an approaching two-dimensional, flat plate, turbulent boundary layer exiting the combustor. These idealized conditions are generally not possible given the nature of the combustor design that often contains large dilution holes, film-cooling holes along the approaching liner, and some type of leakage juncture at the combustor-turbine interface. This type of combustor design produces nonuniformities near the platform in both the span (radial) and pitch (circumferential) directions with large levels of turbulence in the mainstream.

This paper is the second of a two-part series (Colban et al. [1]) that investigates the effects of a range of combustor liner flows on the first vane heat transfer, flow fields, and thermal fields. Part 1 presented a discussion of the inlet conditions that were simulated as well as the adiabatic wall temperatures measured along the platform. Part 2 presents flow and thermal field measurements for selected cases of interest. In general, the objectives for the work presented in this paper were the following: i) to evaluate the effect of non-uniform inlet conditions on the formation of what has been commonly known as the leading edge horseshoe vortex, ii) to evaluate the effect of increasing the liner coolant flow at the vane stagnation, and iii) to evaluate the effect of increasing the slot flows on the secondary flow development. These effects will be presented in terms of measured flow and thermal fields. While the relevant past literature and test facility were discussed in Part 1, some details will be presented on how the velocity and temperature fields were measured. Finally, measured results are presented.

Experimental Facilities and Instrumentation

As discussed in Part 1, the experiments for this study were performed in a low-speed, closed-loop wind tunnel that housed a combustor simulator and a downstream turbine vane. The data was acquired for large-scale models of the combustor and vane to allow for good measurement resolution. The test cases that were investigated for this study are repeated from Part 1 in Table 1 for clarity.

Flowfields were measured for two planes that included a stagnation plane (SP) and one suction side plane (SS2). The suction side plane was orthogonal to the vane surface, as shown in Fig. 1, to discern the secondary flows. Note that Kang and Thole [2] previously presented flow field results for the same vane geometry in a number of planes, including SP and SS2, for an approaching turbulent boundary layer along the platform. This previous study will be used for comparisons to the data presented in our paper. Two-component measurements (u and w) were measured for the SP plane while three-component measurements were made for the SS2 plane. The three-component measurements were made by positioning the two-component fiber optic probe of the laser Doppler velocimeter (LDV) system in two different orientations.

The back-scatter fiber optic LDV system used in this study consisted of a 5-W laser used in conjunction with a TSI model 9201 Colorburst beam separator. Velocity data was processed using TSI model IFA 755 Digital Burst Correlator controlled using TSI's FIND software. Two different focusing lenses were used for these measurements. For the SP plane, a 750-mm focusing lens with a beam expander was used. For the SS2 plane a 350-mm focusing lens without a beam expander was used to make measurements of the streamwise (u) and pitchwise (v) components through the top endwall. The spanwise component (w) was measured from the side also using a 350-mm focusing lens. The probe volume length and diameter for the 350-mm lens were 1.3 mm and 90 microns whereas the probe volume length and diameter for the 750-mm lens with the beam expander were 0.85 mm and 46 microns. For each component of velocity 20,000 data points were used to compute the mean and turbulent quantities. The flow was seeded using 1 micron diameter olive oil particles. The data were corrected for velocity bias effects by applying the residence time weighting. The thermal field measurements were made using a Type E thermocouple that was placed on a traversing unit.

Uncertainty Estimates. The partial derivative and sequential perturbation methods, described by Moffat [3], were used to estimate the uncertainties of the measured values. Uncertainties were calculated based on a 95% confidence interval. The estimates of uncertainties on each of the values presented in this paper are

Contributed by the International Gas Turbine Institute and presented at the International Gas Turbine and Aeroengine Congress and Exhibition, Amsterdam, The Netherlands, June 3–6, 2002. Manuscript received by the IGTI January 16, 2002. Paper No. 2002-GT-30527. Review Chair: E. Benvenuti.

Table 1 Percentage of coolant based on exit mass flow (jet momentum flux ratios are in parentheses)

Case	1	2	3	4	5
Panel 1	1.5 (15.6)	1.5 (17.3)	1.5 (19.7)	1.5 (16.8)	1.5 (18.4)
Panel 2	3.5 (12.3)	3.5 (13.7)	3.4 (15.1)	3.5 (13.3)	3.5 (14.5)
Panel 3	3.4 (7.7)	4.5 (13.9)	5.4 (21.6)	4.5 (13.6)	4.5 (14.4)
Panel 4	1.6 (2)	2.7 (5.5)	3.7 (10.3)	2.7 (5.4)	2.7 (5.6)
Dilution 1	8.8 (130)	8.3 (128)	7.9 (128)	8.3 (125)	8.3 (136)
Dilution 2	8.8 (33)	8.5 (33)	8.2 (33)	8.5 (32)	8.5 (34)
Slot	0.63	0.63	0.63	0.315	1.26

given in Table 2. Note that the uncertainty estimates were made for the near endwall region where the highest uncertainties arise. Also note that the definitions of these variables will be provided later in the text (refer to Fig. 3). The uncertainty for the normal velocity (V_n) was significantly higher than the other velocity components and primarily arose from the uncertainty in the flow angle at the midspan location. For V_n, both u and v velocity components contributed with neither dominating. In comparison for V_s, the term $u \cos \psi_{ms}$ is quite large with the u -component dominating. While for V_s the uncertainty was dictated by the uncertainty in the u-component, the uncertainty for V_n was dictated by the uncertainty in ψ_{ms}

Flow Quality and Analysis for the SS2 Plane

As a check on the flow quality in the spanwise direction, total pressure profiles were measured downstream of the step at the vane midpitch and just off the suction side surface of the vane in the SS2 plane. These total pressures were measured for case 2 using a Kiel probe and were normalized as shown in Fig. 2. For both planes, the flow is quite symmetric with only slightly different values occurring near the wall. The reason for the differences in magnitude near the wall is because the flow exiting the slot is highly sensitive to the interaction between the feed holes and pin fins. This sensitivity of the total pressure profile on the interaction between the feed holes and pin fins was previously reported by Barringer et al. [4]. These profiles indicated a very non-periodic pattern. Any slight differences between the feed hole alignment and the downstream pin fins will cause a range of differences in the total pressure exiting the slot.

In general, the total pressure measurements taken at the midpitch inlet plane (between the two vanes), shown in Fig. 2, indicate very low total pressure values near the platform with a peak in total pressure at nominally 10% span. The high values correspond to the higher total pressure of the film-cooling flow while the low total pressure values correspond to the slot flow in this region. Very little flow is exiting the slot at the mid-pitch region, as was shown in Part 1 from the adiabatic effectiveness measurements.

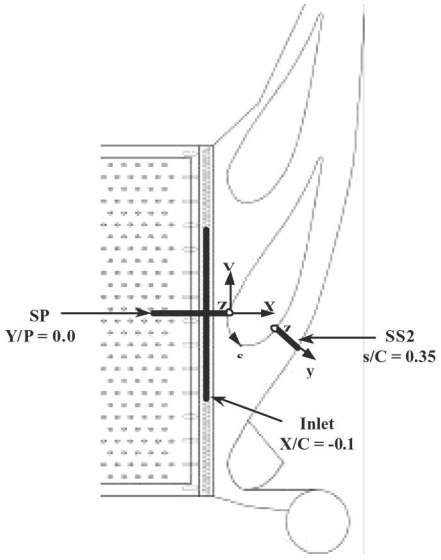

Fig. 1 Locations of flow and thermal field measurements

As the flow progresses through the vane passage, a strong passage vortex develops that is able to sweep high pressure film-coolant fluid down towards the endwall. This vortex will be shown later in this paper. As a result of this sweeping motion, the total pressure in the near-wall region is higher than the slot exit flow (shown in Fig. 2). Moving away from the endwall the total pressure decreases whereby the minimum level corresponds to the center of the passage vortex. Above the minimum level, there is again an increase in total pressure as a result of the film-cooling as indicated in Fig. 2. Most of the midregion is nearly uniform at a total pressure level less than the peak value.

The primary interest of this study was to discern the secondary flows convecting through the turbine vane passage in the SS2 plane. The velocity vectors of these vortices, which will be referred to as the secondary flow vectors, were determined by transforming the measured local velocities (u, v, and w) into the mean flow direction based on that occurring at the midspan (V_s, V_n, and V_z). These velocity components are illustrated in Fig. 3. For this transformation the inviscid turning angle was calculated based on the measured velocities at the vane midspan (u_{ms} and v_{ms}) using the following relation:

$$\psi_{ms} = \tan^{-1}(v_{ms}/u_{ms}) \tag{1}$$

The local transformed velocities are then calculated from the following:

$$V_s = u \cos \psi_{ms} + v \sin \psi_{ms} \tag{2}$$

$$V_n = -u \sin \psi_{ms} + v \cos \psi_{ms} \tag{3}$$

$$V_z = w \tag{4}$$

where u and v are the locally measured velocities. The secondary flow vectors are plotted using the components normal to the mean flow direction (V_n, V_z).

Stagnation Plane Flow Field

Langston's [5] depiction of the secondary flows is comprised of a leading edge horseshoe vortex and passage vortex. This depic-

Table 2 Uncertainty estimates for measurements

θ	$\pm$4.4% at $\theta = 0.9$ $\pm$12.3% at $\theta = 0.3$
V_s	$\pm$1% near vane-endwall
V_n	$\pm$7.5% near vane-endwall
V_z	$\pm$1.5% near vane-endwall
Tu	$\pm$2.4% near vane-endwall
ϕ	$\pm$1% near vane-endwall
$\frac{P_o - P_{o,ms}}{0.5\rho U_{in}^2}$	$\pm$1.6%

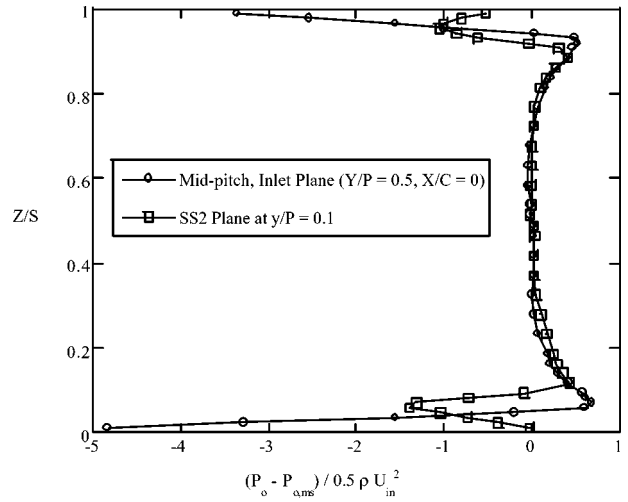

Fig. 2 Total pressure measurements at two locations indicating the midspan symmetry

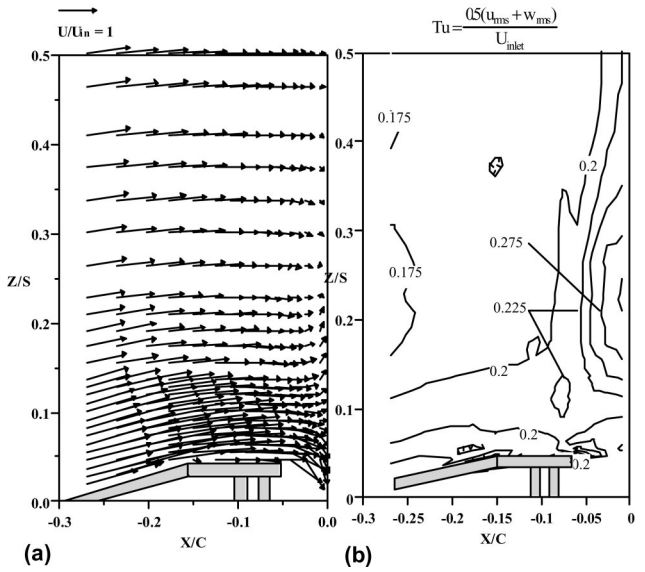

Fig. 4 Measured mean (*a*) and turbulent (*b*) velocities at the stagnation plane for case 2 with a nominal total pressure peak and nominal slot flow conditions

tion was in agreement with his own measurements as well as those reported by Kang et al. [6] and Kang and Thole [2] for the same vane geometry reported in this paper. Note, however, his model and those measurements were for an approaching turbulent boundary layer along the upstream platform. For the geometry of a backward-facing slot reported in our paper, the incoming total pressure profile produced is quite different than that of a flat plate, turbulent boundary layer.

The measured mean and turbulent velocity fields in the SP plane for case 2, as described in Part 1 (nominally peaked total pressure profile above the slot and nominal slot flow), are shown in Figs. 4(*a*, *b*). The velocity vectors indicate flow moving up the combustor liner wall with no indication of any type of separation on the top of the step. Unlike that for an approaching turbulent boundary layer along the endwall, there is no roll-up of a leading edge horseshoe vortex on top of the combustor liner. It was not possible to acquire flow field measurements below the step because of optical accessibility, but based on the CFD predictions shown in Part 1 there is a confined vortical roll-up under the slot area.

The vectors shown in Fig. 4(*a*) also indicate slightly slower velocities in the 15–30% span region than at the wall or platform. The larger velocities near the wall are a result of the film-cooling injection and the acceleration along the liner wall. At the end of the step, there are strong downward velocities indicated as the mainstream fluid is pulled into the slot region. This ingestion into the slot was also previously predicted using CFD, as shown in Part 1 of this paper. Note, however, the CFD analysis was conducted for case 1 in which the total pressure profile above the step was relatively flat. For the data shown in Fig. 4(*a*), there was a slightly higher peak in the total pressure profile due to the film-cooling (case 2).

Another important feature of the flow as it approaches the stagnation location is that there are a number of flow splits that occur. These flow splits occur where the *w*-component of the velocity changes direction from a positive value (indicating flow toward the midspan) to a negative value (flow toward the endwall). These flow splits can more easily be shown by examining profiles of the *w*-component of the velocity as shown in Fig. 5. At the location farthest from the vane ($X/C=-0.06$), most of the velocities are nearly zero except near the wall. Approaching the wall from the midspan indicates slightly negative velocities followed by an inflection point with a tendency toward positive velocities. The negative velocities are a result of the fluid being pulled into the slot whereas the positive, near-wall velocities are a remnant of the flow following the liner wall.

Moving closer to the vane, the *w*-component profiles shown in Fig. 5 indicate several inflection points at locations of $Z/S=0.1$ and 0.23. Moving toward the midspan near the $Z/S=0.1$ location, the *w*-component indicates the flow is switching sign from negative to positive values. This results in a flow split. Moving toward the midspan near the $Z/S=0.026$ location, the *w*-component indicates the flow is switching sign from positive to negative values. This results in a flow impingement, as also seen by the vector plot in Fig. 4(*a*). The total pressure profile above the slot as in Part 1 for case 2, can be used to explain the flow splits.

In general, the turbulence levels in the stagnation plane, presented in Fig. 4(*b*) are quite high as a result of the dilution flow. The levels are 17.5% in a majority of the midspan region. The highest turbulence levels, of nearly 30%, occur in the region of the previously described flow impingement location. The turbulence in this region is even higher than that near the wall due to the film-cooling flow.

Because the flow in the stagnation region, particularly in the 10–30% span region had such high turbulence levels, the probability density functions (PDFs), also known as histograms, were analyzed. PDFs indicate the number of occurrences of a particular velocity level in a given bin size. The equation for the PDFs is given by

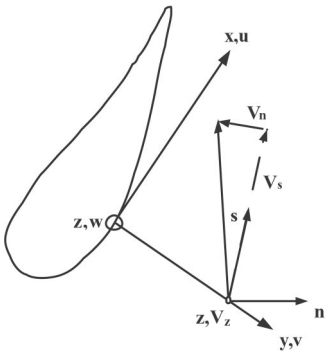

Fig. 3 Measured and transformed velocity components

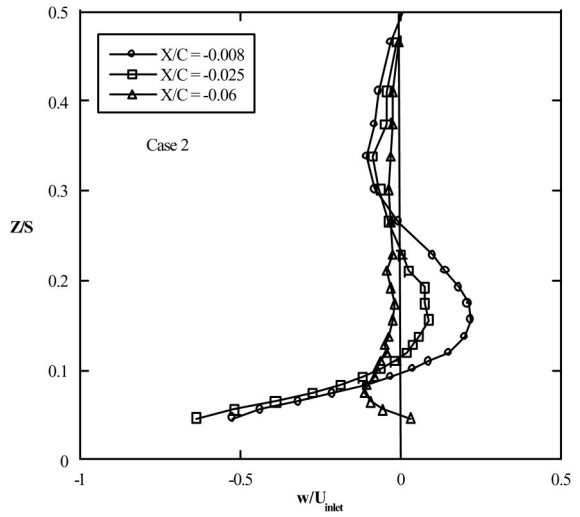

Fig. 5 Measured *w*-component velocities at the stagnation plane (SP) for case 2 with a nominal total pressure peak and nominal slot flow conditions

$$\mathrm{PDF}(w/U_{\mathrm{inlet}}) = \frac{N_i}{N}\frac{1}{\Delta w/U_{\mathrm{inlet}}} \tag{6}$$

where N is the total number of data points and N_i is the number of occurrences in a given $\Delta w/U_{\mathrm{inlet}}$ bin size. For most turbulent flows, the PDFs indicate a Gaussian distribution of the velocities whereby the range of velocities is $\pm 3w_{\mathrm{rms}}$.

As discussed, there were two different flow field phenomena occurring along the stagnation location. First, there is a flow split that happens when the velocity vectors are directed away from the same location. This split occurs at $Z/S=0.1$ as shown in Fig. 4 as the *w*-component changes from negative to positive (moving away from the endwall). Second, there is a flow impingement when the velocity vectors are directed toward the same location. This impingement occurs at $Z/S=0.26$ as the *w*-component changes from positive to negative. The PDFs for several positions along the span of the vane are shown in Fig. 6. The velocity PDFs reveal that the turbulence in the region of the flow split has a single peak with a nearly Gaussian distribution. In the region of a flow impingement, however, the PDFs indicate a bi-modal distribution. This bi-modal distribution is an indication that the flow is very unstable in this region. It is quite plausible that a flow impingement at low velocities is very unstable. These results also lead us to believe that the high levels of turbulence in the 20% span region are because of the flow instability that occurs. The flow instability, in turn, can be promoted by the high levels of turbulence as well.

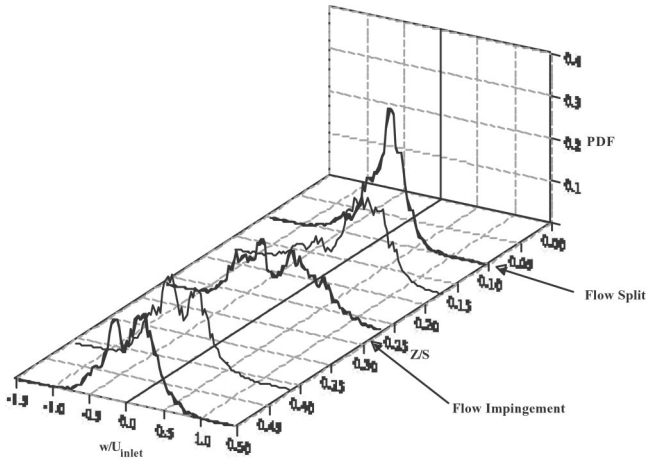

Fig. 6 PDFs of w/U_{in} component of the velocity along the vane stagnation location ($X/C=-0.008$) for case 2

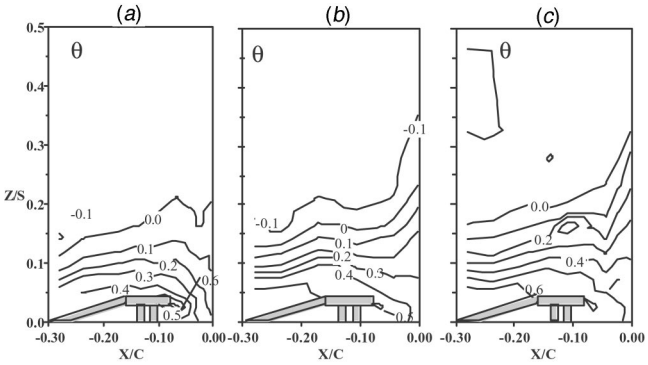

Fig. 7 Contours of normalized temperatures (θ) in the stagnation plane for case 1 (*a*), case 2 (*b*), and case 3 (*c*)

Stagnation Plane Thermal Fields

The thermal fields were measured for three different flow cases to illustrate the effect of increasing the film-cooling liner flow (cases 1–3) while maintaining the same nominal slot flow conditions. The measured thermal fields for these cases are shown in Figs. 7(*a-c*). The temperatures were normalized using the mass-averaged inlet temperature at the vane entrance. In some instances, the θ values are negative in the midspan. The reason for these negative values is because of the large amount of coolant that is injected into the main gas path. As a result of the added coolant, the mass-averaged temperature is cooler than the heated midspan fluid.

The thermal fields illustrated in Figs. 7(*a-c*) show that the film-cooling flow has significantly increased from case 1 to case 3 as indicated by lower temperatures (higher nondimensional temperatures) on top of the liner. Two detrimental effects are apparent from these thermal field measurements with regards to the vane endwall. First, with an increase in liner coolant there is also an increase in the amount of the cooling flow that is being transported along the vane span. Much of the coolant is being transported along the vane span away from the endwall. It is apparent that the $\theta=0.1$ contour moves from being pulled into the slot for case 1 to being pushed up the vane span to a location of $Z/S=0.17$ for case 3. These contour plots contradict the desired result of cooling the endwall surface by adding more coolant from the liner holes. Second, as the liner cooling is increased the coolant ingested by the slot becomes relatively cooler.

As the film-cooling jet injection increases, the driving pressure between the jets and the mid-span flow increases, as well as the driving pressure between the jets and the slot flow. Based on the thermal field measurements at the vane stagnation, however, there is a larger increase in the transport of the film-cooling flow up the vane stagnation as the liner film-cooling flow is increased. The thermal field results, along with the adiabatic effectiveness results in Part 1 do indicate that the flow inside the slot is mixed with the film-cooling flow before exiting the slot. This results in overall higher temperatures (lower θ values) exiting the slot

Passage Flows as Affected by the Slot Flow

As previously discussed, the flow fields were mapped in the SS2 plane for the nominal slot flow (case 2) as well as the double slot flow (case 5) cases. Prior to making the velocity transformations, the flow field at the mid-span was compared with a three-dimensional, viscous CFD prediction for the design slot flow con-

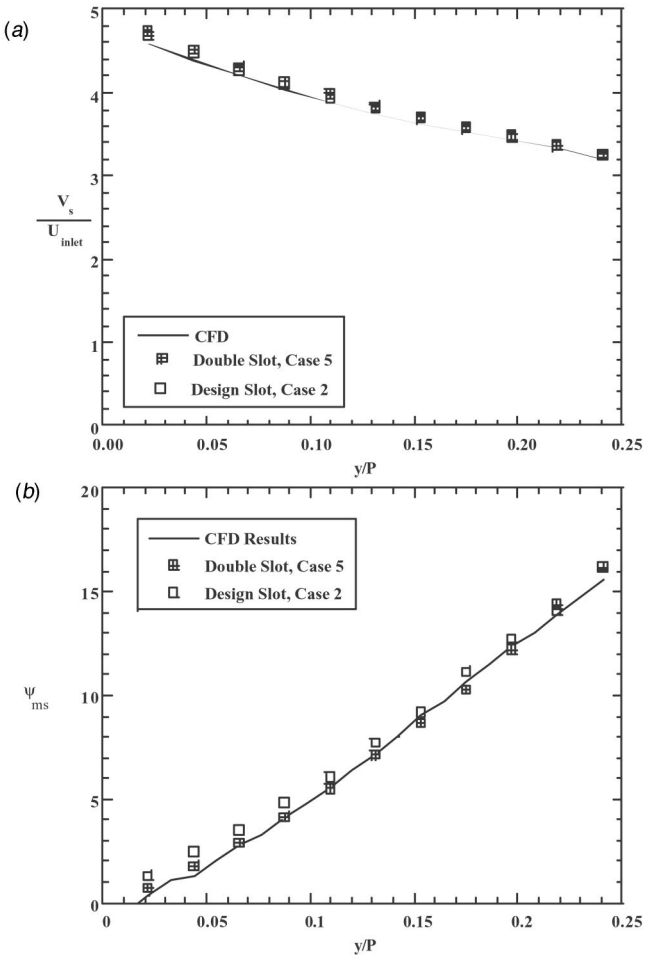

Fig. 8 Comparison of the measured and predicted streamwise velocity component (*a*) and flow turning angle (*b*) at the midspan SS2 location for case 2

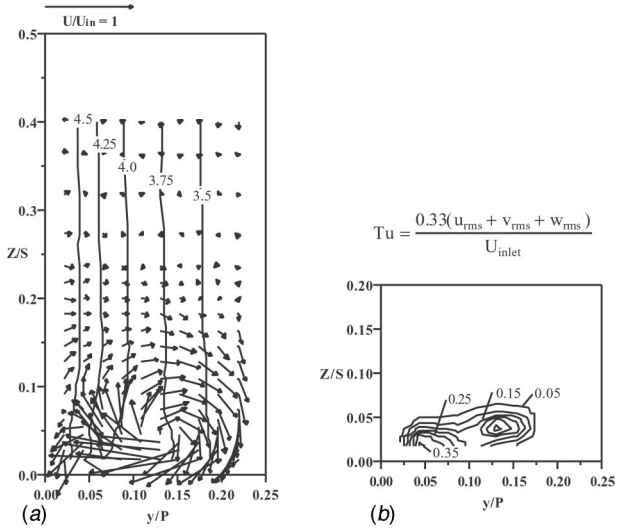

Fig. 9 Measured streamwise velocity contours (V_s / U_{inlet}) along with secondary velocity vectors (*a*) and turbulence level contours (*b*) for an inlet turbulent boundary layer [2] for the SS2 plane

ditions (case 1). Note the CFD prediction will be presented in a later publication. Figures 8(*a*, *b*) show the predicted and measured streamwise velocity component and flow turning angle at the midspan location for the SS2 plane. Good agreement was found between the prediction and measurements across the pitch for both the slightly peaked total pressure profile with the nominal slot flow (case 2) as well as the double slot flow (case 5).

As a point of reference, it is important to show the resulting secondary flow field for a case with an inlet turbulent boundary layer along the upstream endwall for this same vane geometry as reported by Kang and Thole [2]. Note that the boundary layer thickness just upstream of the vane was $\delta/S=0.1$ for their study. The secondary flow field for the inlet condition of a turbulent boundary layer is shown in Fig. 9(*a*). Superimposed on the secondary flow vectors are contours of the streamwise velocity component. At the SS2 location, the maximum streamwise velocity has accelerated by a factor of 4.75 over that of the inlet velocity. The secondary velocity vectors show remnants of the suction side leg of the horseshoe vortex at the suction side-endwall corner (near $y/P=0$) and the dominant passage vortex. Downward turning flow is apparent as high as 20% of the vane span as a result of the passage vortex. The center of the vortex is located at approximately $y/P=0.12$. The turbulence levels for the SS2 plane are shown in Fig. 9(*b*) for the inlet turbulent boundary layer. These turbulence levels are quite high near the endwall and show two peak levels that correspond with the suction side leg and passage vortices.

In contrast to the case with a turbulent boundary layer, Fig. 10(*a*) shows the measured secondary flows for the case with the nominal slot and film-cooling flows (case 2). The streamwise velocity contours indicate a slightly larger effect of the secondary flows on the streamwise velocities for case 2 as compared with the turbulent boundary layer conditions (shown in Fig. 9(*a*)). The secondary flow fields shown in Figs. 9(*a*) and 10(*a*) are clearly different. Any remnants of a suction side leg of a horseshoe vortex are essentially very small at this location for case 2 as compared with the turbulent boundary layer case. While the passage vortex is still present for both cases, the location of this vortex has shifted toward the suction side of the vane with the center being located closer to $y/P=0.08$. The overall strength of the passage vortex has increased in Fig. 10(*a*) relative to the data shown in Fig. 9(*a*) while the extent in the span direction was reduced to be below $Z/S=0.12$.

The most noticeable difference between Figs. 9(*a*) and 10(*a*) is the appearance of a counterclockwise vortex located off of the endwall surface that is driving flow up the pressure side of the

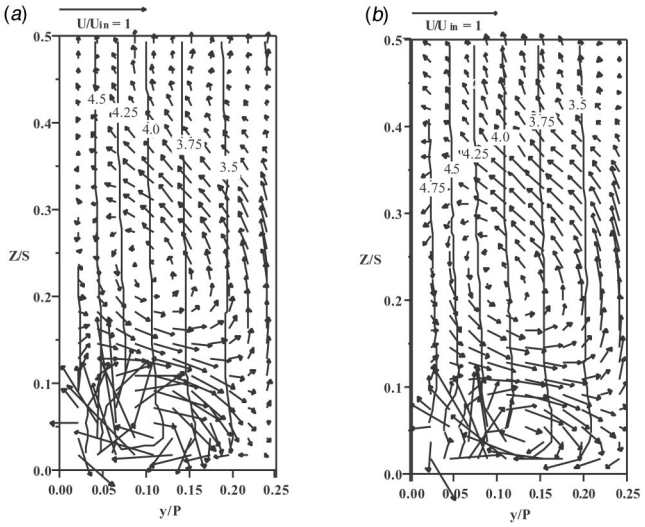

Fig. 10 Measured streamwise velocity contours (V_s / U_{inlet}) along with secondary velocity vectors for case 2 inlet conditions (*a*) and case 5 inlet conditions (*b*)

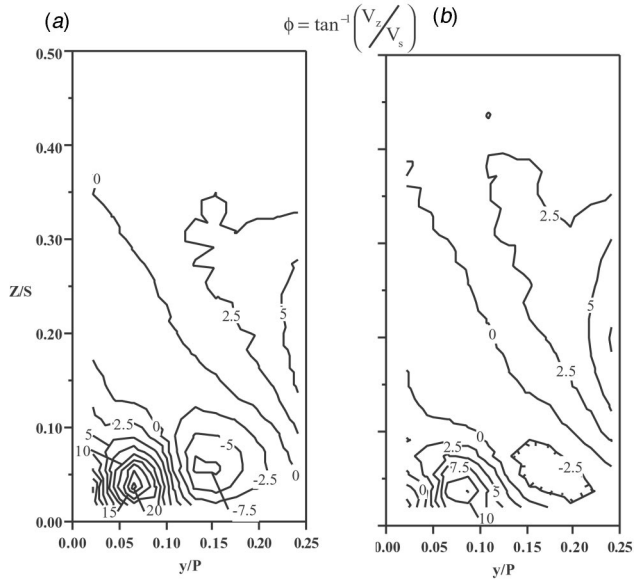

Fig. 11 Contours of the pitch angle(ϕ) in the SS2 plane for cases 2 (*a*) and 5 (*b*)

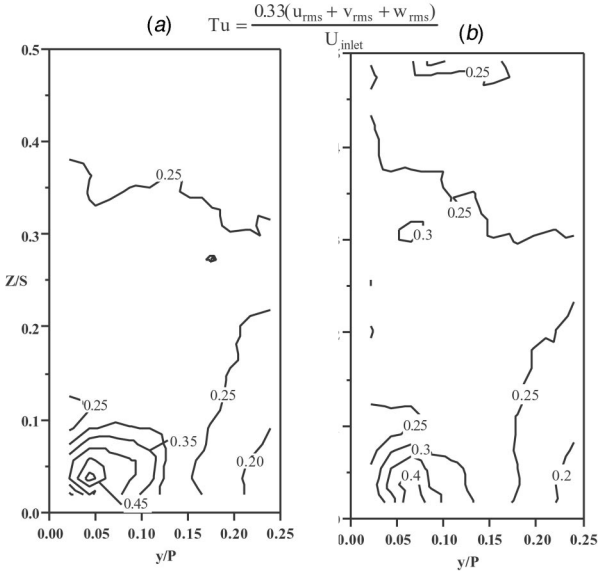

Fig. 12 Contours of turbulence in the SS2 plane for cases 2 (*a*) and 5 (*b*)

adjacent vane and down the suction side of the vane. The center of this counter-rotating vortex is only slightly closer to the pressure surface than the passage vortex. The flow split along the suction side is located at $Z/S=0.17$ while the flow split along the pressure side is located at $Z/S=0.05$. The formation of the counter-rotating vortex shown in Fig. 10(*a*) is a result of the total pressure profile previously discussed. The higher total pressure from the film-cooling jets on top of the liner step along with the slightly lower total pressure in the mainstream results in a driving pressure difference. This pressure difference results in a counter-rotating vortex pattern. Although this counter-rotating vortex was computationally predicted by Hermanson and Thole [7] for an inlet condition of a peaked total pressure near the platform, there have been no experimental studies to validate its existence.

Figure 10(*b*) shows the effect of doubling the slot flow on the secondary flow field. While the streamwise velocity contours are almost the same as the nominal slot flow condition (case 2), there are some effects on the secondary flow field. The strength, size, and position of the passage vortex have been altered for the double slot flow case. The strength and size are reduced as a result of the higher total pressure exiting the slot for the double slot flow case. Alternatively, the counter-rotating vortex strength has increased in magnitude. This increase in the counter-rotating vortex is because of a reduced competing effect to drive the flow towards the platform due to the higher slot flow pressure.

To illustrate the stronger turning for the nominal slot flow case (case 2) relative to the double slot flow case (case 5), contours of the pitchwise angle are presented in Figs. 11(*a*,*b*). These contours represent the upward turning angle of the secondary flow vectors. The contours of the pitch angles in Fig. 11(*a*) indicate much larger turning angles on both legs of the passage vortex for case 2 as compared with Fig. 11(*b*) for the double slot flow case 5.

The turbulence level contours for the nominal and double slot flow cases are shown in Fig. 12(*a, b*), respectively. The characteristics of the turbulence overall are much higher than the turbulent boundary layer approach shown in Fig. 9(*b*). The freestream turbulence level, due to the dilution jets, for the flow fields given in Figs. 12(*a*) and (*b*) indicate levels between 25 and 30%. Recall that the velocity has also increased by over 3.25 to 4.75 times that of the inlet velocity meaning that the turbulence level based on the local velocity is closer to 5.5%.

The peak turbulence levels in Figs. 12(*a*) and (*b*) correspond to the upward leg of the vortex in all of the cases including that shown in Fig. 9(*b*). There are two noticeable differences, however, in comparing the turbulent inlet profile case to the cooled liner/slot cases. First, the turbulence levels are as much higher for the cooled liner/slot cases. Second, there is just a single-peaked contour level for the cooled liner/slot cases as compared with a double-peaked contour for the approaching turbulent boundary layer case. Only a single-peaked contour level for the cooled liner/slot cases occurs because the turbulence level of the flow outside the vortices is nearly at the same level of what occurs due to the vortex interaction itself. This fact is illustrated by considering that the turbulence level for the turbulent boundary layer case (Fig. 9(*b*)) has a peak level of $Tu=0.35$. The combustor simulated profiles have turbulence levels above the endwall of $Tu\sim 0.25-0.3$. Since these turbulence levels are nearly the same, we believe that the contour levels would not show a local peak.

Conclusions

The results presented in this paper show the importance of quantifying the proper inlet conditions to the turbine, particularly in the near platform region. Although the secondary flow models that have been proposed previously in the literature are quite helpful in understanding how the flow develops through a first vane passage, these models all have assumed a simple two-dimensional, flat plate, turbulent boundary layer along the endwall. The measurements discussed in this paper provide the first experimental measurements for the effects of a more realistic combustor exit profile on the secondary flow field that develops in the downstream nozzle guide vane.

The flow field measurements at the vane stagnation location indicate no presence of a horseshoe vortex on top of the combustor liner. The flow pattern under the lip of the liner, however, is expected to contain a vortex confined by the lip of the liner and the upstream pin fins. The film-cooling from above the liner is ingested into the slot thereby mixing with the slot coolant. The ingestion ultimately provides a higher exit coolant temperature (lower θ value) resulting in higher adiabatic wall platform temperatures. A number of flow splits and flow impingement points were identified from the flow field measurements as the spanwise velocity component changed direction along the span. The flow impingement location was correlated with a region having relatively low total pressure levels, causing very high turbulence levels. With an increase in the film-cooling flow, there is also an

increase in the local total pressure. The thermal field measurements at the vane stagnation location indicate that there is a significant transport of this coolant away from the endwall and towards the midspan. This results in little thermal benefit to the endwall.

The flow field measurements in the passage for an upstream film-cooled liner/cooling slot configuration indicate a secondary flow pattern much different than that of an approaching two-dimensional turbulent boundary layer. While the suction side leg of the horseshoe vortex is smaller than it is for a turbulent boundary layer, the passage vortex becomes stronger for the liner/slot configuration. In addition, a counter-rotating vortex above the passage vortex was identified. Both of these vortices can be explained by the total pressure variation exiting the combustor. As the liner cooling is increased, the strength and size of the passage vortex were reduced as a result of the higher total pressure exiting the slot. Alternatively, the counter-rotating vortex above the passage vortex increased in strength.

Clearly, the importance of considering the nonuniformities exiting the combustor is critical to predicting the resulting secondary flow field in the nozzle guide vane. The flow angles exiting the nozzle guide vane are an important consideration in designing the rotor. Moreover, in designing the endwall film-cooling hole pattern the secondary flow and thermal fields need to be quantified for the correct combustor exit conditions. The results indicated in this paper also show that coolant exiting a stepped slot upstream of the vane needs to have a high momentum to insure coolant injection rather than hot gas ingestion.

Acknowledgments

The authors are grateful to Pratt and Whitney and the US Air Force Research Lab for their support of this project. In particular, the authors thank Joel Wagner and Matthew Meininger for their contributions of this work.

Nomenclature

C = true chord of stator vane
N = number of data points
p = pitch of stator vane
P_o = total pressure
PDF = probability density function
S = span of stator vane
T = temperature
Tu = turbulence level defined in figures
U, u = mean velocities as defined in Fig. 3
V, v = mean velocities as defined in Fig. 3
V_n, V_s, V_z = secondary velocity components to inviscid flow direction
W, w = mean velocities as defined in Fig. 3
X, x = global and local streamwise coordinate as defined in Fig. 3
Y, y = global and local normal coordinate as defined in Fig. 3
Z, z = global and local spanwise coordinate as defined in Fig. 3
δ = boundary layer thickness (99% edge)
Δw = bin size for PDF
θ = nondimensional temperature, $(T_{\text{ave}}-T)/(T_{\text{ave}}-T_{\text{cool}})$
ϕ = pitch angle, $\tan^{-1}(V_z/V_s)$
ρ = density
ν = kinematic viscosity
ψ = yaw turning angle at midspan, $\tan^{-1}(v/u)$

Subscripts

ave = mass-averaged
cool = coolant conditions
ms = midspan
inlet = inlet incident velocity
rms = root mean square

References

[1] Colban, W. F., Thole, K. A., and Zess, G., 2002, "Combustor-Turbine Interface Studies—Part 1: Endwall Effectiveness Measurements," ASME J. Turbomach., **125**, pp. 193–202.
[2] Kang, M., and Thole, K. A., 2000, "Flowfield Measurements in the Endwall Region of a Stator Vane," ASME J. Turbomach., **122**, pp. 458–466.
[3] Moffat, R. J., 1988, "Describing the Uncertainties in Experimental Results," Exp. Therm. Fluid Sci., **1**, pp. 3–17.
[4] Barringer, M. D., Richard, O. T., Walter, J. P., Stitzel, S. M., and Thole, K. A., 2001, "Flow Field Simulations of a Gas Turbine Combustor," 2001-GT-0170 to appear in ASME J. Turbomach.
[5] Langston, L. S., 1980, "Crossflows in a Turbine Cascade Passage," ASME J. Eng. Power, **102**, pp. 866–874.
[6] Kang, M., Kohli, A., and Thole, K. A., 1999, "Heat Transfer And Flowfield Measurements In The Leading Edge Region of A Stator Vane Endwall," ASME J. Turbomach., **121**(3), pp. 558–568.
[7] Hermanson, K., and Thole, K. A., 1999, "Effect of Inlet Profiles on Endwall Secondary Flows," J. Propul. Power, **16**(2), pp. 286–296.